Improved Design-Oriented Analytical Modelling of Switched Reluctance Machines Based on Fröhlich-Kennelly Equations

Roberto Rocca, *Member, IEEE*, Giulio De Donato, *Senior Member, IEEE*, Paolo Bolognesi, *Member, IEEE*, Chiara Boccaletti, *Senior Member, IEEE* and Fabio Giulii Capponi, *Member, IEEE*

***Abstract*—Early design stages of modern Switched Reluctance Machines (SRMs) are well-known for demanding the analysis of thousands of candidates. The need for reducing the computation time is, in turn, fostering the interest in design-oriented analytical approaches capable to maintain sufficient accuracy for SRMs featuring different geometries and rated operating conditions. To this end, this work proposes a novel design-oriented analytical model that predicts the flux linkage loci, i.e., a set of curves expressing the phase flux linkage as a function of both phase current and rotor position, from which the main performance are attained. The model comprises two main parts, each of them containing a novel scientific contribution: 1) a new interpolation technique for the flux loci based on second-order Fröhlich-Kennelly equations, and 2) an analytical model that caters for the flux linkage in partial overlap and saturated core conditions. Finally, the model is validated against Finite Element results of four SRMs, along with the experimental results of one of them, and its implementation in a design routine is discussed.**

Index Terms*— *Analytical Model, Flux Linkage, Interpolation Technique, Machine Design, Reluctance, Saturated, Switched Reluctance Machine

I. INTRODUCTION

SWITCHED Reluctance Machines (SRMs) are nowadays considered a promising magnet-free solution for modern applications, such as automotive, aerospace, [1], or kinetic energy storage, [2], [3]. When designing for these applications, the current state of the art relies on strongly automated techniques, mostly supported by Finite Element Analysis (FEA),[1], [4]–[6]. Here, the main inconvenient lies in the fact that thousands of candidates have to be assessed before a final solution is reached, requiring extremely heavy computation burdens. In this scenario, analytical approaches are gaining a steadily growing attention, [1], [7], [8], especially for early design stages where a lower accuracy may be accepted in return for a faster execution, [9].

In a bid to provide a reliable alternative to FEA, design-oriented analytical models should be developed in order to ensure a high accuracy for SRMs featuring any kind of geometry and conceived for different rated operating conditions. The analytical design of any SRM starts from the definition of its flux linkage loci, i.e., a set of curves expressing the phase flux linkage Ψ_{ph} as a function of both phase current i_{ph} and rotor position θ ($\Psi_{ph}(i_{ph}, \theta)$), from which the rest of the performance is calculated, [10]. A schematic example is shown in Fig. 1. The process to define it analytically is usually divided into two subproblems:

1) Choice of an analytical expression of $\Psi_{ph}(i_{ph}, \theta)$, e.g., Polynomials, Fourier Series, etc.
2) Analytical evaluation of the flux linkage values at the desired nodes (pair of values of i_{ph} and θ).

In general terms, the main challenge underpinning both points above is modelling the nonlinear effects of saturation.

With regards of the analytical expression of $\Psi_{ph}(i_{ph}, \theta)$, two approaches are commonly followed, namely Fourier Series and piecewise expressions. For what is concerned with Fourier Series, many contributions agree that this approach suites well the needs of control systems development, whereas its complexity is not ideal for design purposes, [11]–[14]. In terms of piecewise expressions, in [15], flux loci are interpolated by two-linear-piece ones. Here, the main drawback lies in the risk of losing accuracy nearby the knee-point of the saturation curves, so that also this approach does not meet the needs of a design process. Finally, a promising option is the three-nonlinear-piece expression proposed by T.J. Miller in [9], where a set of Ψ_{ph} vs θ curves for constant i_{ph} is defined (see Fig. 1(a)), whose nonlinear parts are interpolated based on first-order Fröhlich-Kennelly (FK) equations, [16]. Although this approach has already proved to suite well the needs of designers, [17], [18], it can be argued that there is still room for improvement. Indeed, when interpolating a nonlinear region (e.g., between θ_2 and θ_u in Fig. 1(a)), a first-order FK equation only offers three degrees of freedom. Consequently, the value of the derivative at one of the region's extremes cannot be set, resulting in non-smooth curves. Moreover, in the way the three-piece formulation is proposed in [9], all rotor positions ranging from θ_a to θ_m (see Fig. 1(a)

(Corresponding author: Roberto Rocca).

Roberto Rocca was with the Department of Astronautical, Electrical and Energy Engineering (DIAEE), "Sapienza" University of Rome, Rome, 00164 Italy. He is now with the Department of Electrical Systems, CIRCE Technology Centre, Zaragoza, 50018 Spain, and with the CIRCE Mixed Research Institute (CIRCE Technology Centre and University of Zaragoza), Zaragoza, 50018 Spain (e-mail: rrocca@fcirce.es).

Giulio De Donato and Fabio Giulii Capponi are with the Department of Astronautical, Electrical and Energy Engineering (DIAEE), "Sapienza" University of Rome, Rome, 00164 Italy. (e-mail: giulio.dedonato@uniroma1.it, fabio.giuliicapponi@uniroma1.it).

Paolo Bolognesi is with Electrical Machines, Power Electronics and Drives Group, DESTEC Department, University of Pisa, Pisa 56122, Italy (e-mail: paolo.bolognesi@ing.unipi.it).

Color versions of one or more of the figures in this article are available online at http://ieeexplore.ieee.org

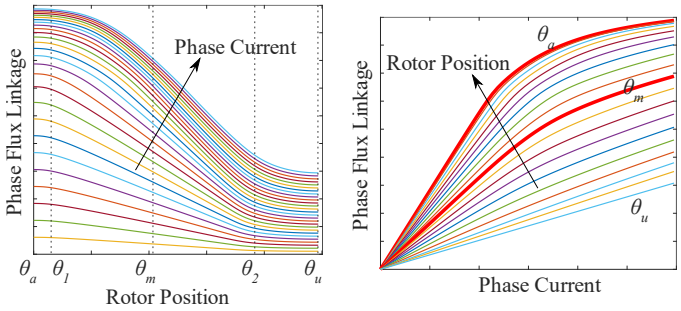

(a) (b)

Fig. 1. Schematic example of flux linkage loci: (a) flux linkage vs. rotor position, (b) flux linkage vs phase current, (the meaning of the rotor positions θ_a, θ_b, θ_m, θ_2 and θ_u is thoroughly explained later in section III).

and Fig. 7) belong to the same "piece". As it is shown later in section V-E, this approach poses the risk of losing accuracy in the vicinity of position θ_1. In bid to tackle the two above issues, this work proposes an innovative piecewise formulation based on 4 pieces, whose nonlinear ones are expressed through a second-order FK equation.

By moving now to the analytical evaluation of the flux linkage values at the desired nodes, the challenge lies in modelling with sufficient accuracy the saturation effects in partial overlap conditions. In [19], this situation is accounted for by dividing stator and rotor teeth into a saturable tip zone and a non-saturable trunk zone. However, no relations between these zones, rotor position and saturation level are clearly defined. Alternatively, [20], [21], divide the stator tooth into a saturable and a non-saturable straight segment, whose thickness changes with the rotor position. However, despite its good accuracy, this approach results quite complex for design purposes. In [17], [22], a multi-branch magnetic circuit is proposed, where flux tubes' geometries are defined by tracing the contour plots obtained with FEA. Consequently, the effort for a first implementation is considerable. Moreover, flux tubes shapes may change significantly from one SRM to another, so that this approach might not guarantee the the versatility needed in a design process. Finally, [23] develops a 3-reluctance network with one representing the teeth saturation. However, also in this work no relation between geometry, rotor position and saturation level is clearly defined. In a bid to fill this gap found in the literature, this work proposes a novel analytical model based on the numerical solution of Ampere's and Gauss' equations, formulated by representing the flux tubes inside stator and rotor teeth with a hyperbolic tangent shape. Here, it is important to highlight that with the 4-piece formulation proposed for the $\Psi_{ph}(i_{ph}, \theta)$ loci, it is sufficient to evaluate the saturated flux linkage only at the mid-way position θ_m (see Fig. 1(a)). Hence, only this position is considered in this work.

This paper is organised as follows. Section II provides an overview of design-oriented analytical modelling of SRMs. Section III presents the unsaturated inductance profile. Section IV and V are devoted respectively to the description of the analytical formulation of the saturated flux linkages and the $\Psi_{ph}(i_{ph}, \theta)$ curves. Finally, section VI validates the proposed model and discusses its use in a design routine.

II. Design-Oriented Analytical Modelling of SRMs

A. General Background

An example of SRM candidate is provided in Fig. 2, whose geometric variables are listed in TABLE I. The first step in modelling the performance of an SRM candidate is usually the definition of its $\Psi_{ph}(i_{ph}, \theta)$ loci. Subsequently, under the widely accepted assumption of mutually decoupled phases, the static torque loci, $T_{sta}(i_{ph}, \theta)$, of one phase are evaluated by means of the energy/coenergy theory as in (1), [24], where the integral refers to one stroke undergone by one phase:

$$T_{sta}(i_{ph},\theta) = \frac{\partial}{\partial\theta}\left(\int_0^{i_{ph}} \Psi_{ph}(i_{ph},\theta)\, di_{ph}\right) \tag{1}$$

Then, by keeping the assumption of magnetically decoupled phases, the phase voltage equation can be solved to obtain the variation over time of i_{ph} and θ during one stroke, [10]:

$$\begin{cases} v_{ph}(t) = R i_{ph}(t) + \dfrac{d}{dt}\left(\Psi_{ph}\left(i_{ph}(t),\theta(t)\right)\right) \\ \theta(t) = \omega\, t \end{cases} \tag{2}$$

Here, v_{ph} denotes the instantaneous phase voltage imposed

TABLE I
Geometric Parameters of a SRM Design Candidate

Symbol	Parameter	Symbol	Parameter
ζ_s	Stator Pitch Angle	P	Number of Stator Teeth Pairs per Phase
ζ_r	Rotor Pitch Angle	h_{st}	Stator Tooth Height
β_{st}	Stator Tooth Angle	h_{rt}	Rotor Tooth Height
β_{rt}	Rotor Tooth Angle	L_{stk}	Axial Stack Length
A_{ss}	Slot Area	l_g	Air gap Thickness
D_s	Stator Bore Diameter	m	Number of SRM phases
D_r	Rotor Outer Diameter	b_{sy}	Stator Yoke Thickness
b_{ry}	Rotor Yoke Thickness		

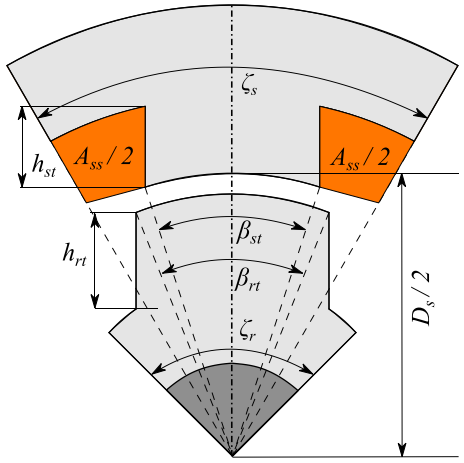

Fig. 2. Example of geometry an arbitrary SRM candidate.

by the converter and ω the speed of rotation, which is normally kept constant at a desired design point. Then, as (2) is solved, $i_{ph}(t)$ and $\theta(t)$ can be plugged into (1) to obtain the instantaneous phase torque waveform $T_{ph}(t)$. Finally, contributions provided by the remaining phases can be found by properly shifting $i_{ph}(t)$ and $T_{ph}(t)$ with respect of θ.

Regarding the hypothesis of negligible mutual coupling effects, it is reminded that this last is normally accepted in early design stages, although its verification is necessary in more advanced stages.

B. Design Candidate Performance Prediction

In the case of this work, the background described above is implemented in the design process shown in Fig. 3. As it can be seen, once the geometry of an SRM design candidate is generated (this aspect is not addressed in this work), the first step to take is the phase unsaturated inductance vs. rotor position profile evaluation. This task is described in section III. Once the unsaturated inductance profile is determined, the flux linkage vs. phase current at fully aligned and mid-way positions are calculated (see curves marked in red in Fig. 1(b)) in the way outlined in section IV. As it can be seen in Fig. 3, aligned and mid-way saturated flux linkages feed the "Flux Loci Calculator". Here, the flux linkage loci are evaluated through the interpolation process proposed in this work, which is described in section V. At this point, as the flux linkage loci are available, both (1) and (2) are resolved in the "Performance Calculator" block, obtaining the $T(t)$ and $i_{ph}(t)$.

III. Unsaturated Inductance Profile

By following Fig. 3, modelling begins from the unsaturated inductance profile.

A. Profile's Regions Definition

An example of unsaturated phase inductance vs. rotor position profile is shown in Fig. 4. As it is typically done for SRMs, it represents the incremental self-inductance of one phase $L_{ph}{}^{u}(\theta)$. The idea proposed in this work is to model this curve by dividing it into four regions, as also represented in Fig. 4. The initial rotor position θ_a is considered at the full alignment between one stator and one rotor tooth, as shown in Fig. 5(a). As the rotor moves, two facing poles remain fully overlapped until the tip-to-edge position θ_1 (Fig. 5(b)), where Region I terminates. Then, Region II begins as stator and rotor partially overlap. The centre of the partial overlapping zone is referred to as mid-way position θ_m, where just half stator tooth overlaps with the rotor (Fig. 5(c)). From θ_m onwards, the rest of the partial overlap zone defines Region III, which ends at the tip-to-tip position θ_2 (Fig. 5(d)). Finally, Region IV describes the non-overlap zone up to the full unalignment condition θ_u, which is sketched in Fig. 5(e).

B. Second-Order Fröhlich-Kennelly Equation

As it can be seen in Fig. 4, Region IV shows a nonlinear trend. As said above, for modelling nonlinear parts this work proposes a second-order FK equation, as it is shown below:

$$L_{ph}{}^{u}(\theta) = L_x + \frac{a_x\, b_x\, (\theta - \theta_x)^2}{a_x + \theta - \theta_x} \tag{3}$$

Here, it is important to underline that this formulation possesses four degrees of freedom: L_x, a_x, b_x and θ_x, which, in turn, allow one to set four boundary conditions. These last may be the values of the inductance at both extremes of one region, along with the derivative values, in such way as to attain a perfectly smooth curve. A more in-depth discussion about the proposed formulation is provided in subsection V-D.

C. Unsaturated Inductance Profile

To define the unsaturated inductance profile, the initial task is the evaluation of the unsaturated inductances corresponding to the five rotor positions mentioned above:

$L_a{}^u$: Unsaturated aligned inductance, at $\theta = \theta_a$,
$L_1{}^u$: Unsaturated tip-to-edge inductance, at $\theta = \theta_1$,
$L_m{}^u$: Unsaturated mid-way inductance, at $\theta = \theta_m$,
$L_2{}^u$: Unsaturated tip-to-tip inductance, at $\theta = \theta_2$,
$L_u{}^u$: Unsaturated unaligned inductance, at $\theta = \theta_u$.

In this work, $L_a{}^u$, $L_2{}^u$ and $L_u{}^u$ are evaluated directly from the SRM geometry through the analytical technique proposed in [24], which is based on a permeance approach representing the magnetic flux tubes with an elliptic shape. Besides, $L_1{}^u$ and $L_m{}^u$ are calculated by the well-established assumption that in absence of saturation the inductance profile is constant between θ_a and θ_1 and descends linearly from θ_1 to θ_2:

$$L_1{}^u = L_a{}^u \tag{4}$$

$$L_m{}^u = L_a{}^u - \frac{L_a{}^u - L_2{}^u}{\theta_2 - \theta_1}\,\theta_m \tag{5}$$

At this point, all regions can be defined. Thanks to the assumption of neglecting fringing and rounding phenomena, Region I is modelled through a constant inductance value equal to $L_a{}^u$. Subsequently, Regions II and III are modelled together assuming that the profile decays linearly until position θ_2. Then, Region IV begins, whose profile is obtained via (3), by applying the boundary conditions in (6). Here, the first derivative constraint imposes that the profile reaches its minimum point at full unalignment while the second one sets the slope at θ_2 equal to that of Region III. The need to define the unsaturated profile is clarified in the description of

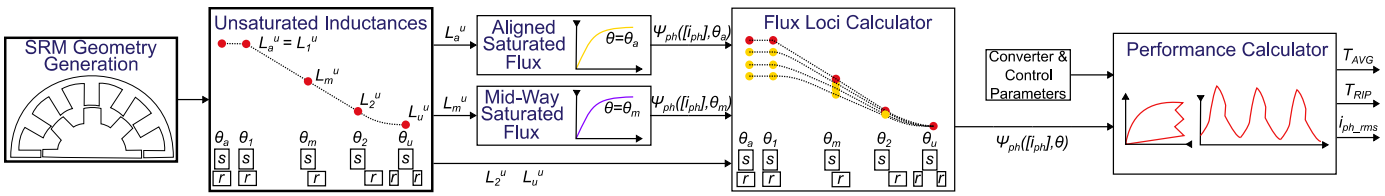

Fig. 3. High-Level overview of the analytical SRM performance prediction process used in this work.

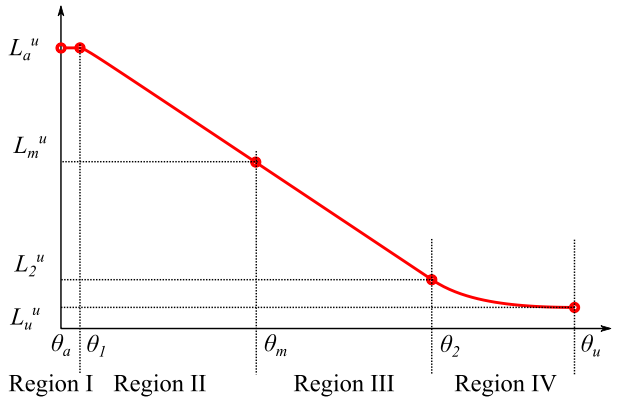

Fig. 4. Example of inductance vs rotor position curve in unsaturated conditions.

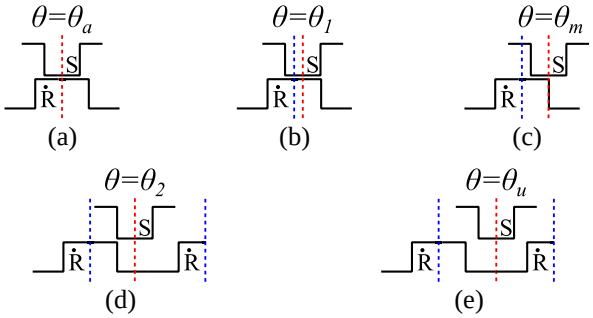

Fig. 5. Key Rotor Positions: (a) maximum alignment θ_a; (b) tip-to-edge θ_1; (c) mid-way θ_m; (d) tip-to-tip θ_2; (e) maximum misalignment θ_u.

Regions III and IV in saturated conditions, along with the role of θ_m.

$$\begin{cases} {L_{ph}}^u(\theta_u) = {L_u}^u \\ {L_{ph}}^u(\theta_2) = {L_2}^u \\ \dfrac{d}{d\theta}\left({L_{ph}}^u(\theta)\right)\Big|_{\theta_u} = 0 \\ \dfrac{d}{d\theta}\left({L_{ph}}^u(\theta)\right)\Big|_{\theta_2} = \dfrac{{L_m}^u - {L_2}^u}{\theta_m - \theta_2} \end{cases} \tag{6}$$

IV. Saturated Aligned and Mid-Way Flux Linkages

This section describes the idea proposed for the evaluation of the aligned and mid-way flux linkage curves: $\Psi_{ph}(i_{ph}, \theta_a)$ and $\Psi_{ph}(i_{ph}, \theta_m)$.

Before embarking on the model description, it is highlighted that the formulation used in this work for the $\Psi_{ph}(i_{ph}, \theta)$ loci is based on the definition of a set of continuous functions Ψ_{ph} vs. θ, each for a discrete value of i_{ph} (as illustrated in Fig. 1(a)). Hence, from now on, the following notation is applied: 1) $\Psi_{ph}([i_{ph}], \theta)$, denoting the flux linkage loci obtained for discretised values of i_{ph}, and 2) i_{ph}^*, a given value of i_{ph}.

According to the notation above, the objective in this section is to determine the flux linkages for any i_{ph}^* with the rotor being "locked" respectively at θ_a and θ_m. The outlook of these curves can be seen in the red curves highlighted in Fig. 1(b).

A. Aligned Position

At full alignment, it is widely accepted to model the magnetic circuit as shown in Fig. 6, where grey regions represent the portions of stator and rotor yokes having a non-negligible magnetic voltage drop in saturated conditions (yoke portions corresponding to unsupplied teeth offer very low reluctance due to the wide cross section), [7]. By assuming that the magnetic flux density is uniform within each of the above regions, Ampere's and Gauss' equations can be written as in (7)-(12). Here, (9)-(12) have been expressed by taking the stator tooth cross section A_{st} as a reference for the magnetic flux crossing a stator pole, ϕ_{pole}, neglecting the difference between tooth cross section and area of the tooth face facing the airgap for both stator and rotor (curvature effect).

$$A_{st} = L_{stk}\frac{D_s}{2}\,\beta_{st} \tag{7}$$

$$2N{i_{ph}}^* = 2\frac{B_{st}}{\mu_{st}}h_{st} + 2\frac{B_g}{\mu_0}l_g + 2\frac{B_{rt}}{\mu_{rt}}h_{rt} + \frac{B_{sy}}{\mu_{sy}}l_{sy} + \frac{B_{ry}}{\mu_{ry}}l_{ry} \tag{8}$$

$$B_{rt} = \frac{D_s\,\beta_{st}}{D_r\,\beta_{rt}}\,B_{st} \tag{9}$$

$$B_{sy} = \frac{D_s\,\beta_{st}}{4\,b_{sy}}\,B_{st} \tag{10}$$

$$B_{ry} = \frac{D_s\,\beta_{st}}{4\,b_{ry}}\,B_{st} \tag{11}$$

$$B_g = B_{st}\,K_g(\theta_a) \tag{12}$$

The meaning of the geometrical quantities in (7)-(12) is indicated in TABLE I, whereas new quantities introduced are as follows:

N: Number of series connected turns per stator pole,
B_{st}: Stator tooth average magnetic flux density,
B_{rt}: Rotor tooth average magnetic flux density,
B_g: Mid-Airgap average magnetic flux density,
B_{sy}: Stator yoke average magnetic flux density,
B_{ry}: Rotor yoke average magnetic flux density,
$K_g(\theta_a)$: Airgap factor at aligned position,
μ_i (B_i): Magnetic permeability of the ith circuit part,
l_{sy}: Stator yoke active path length (grey zones in Fig. 6),
l_{ry}: Rotor yoke active path length (grey zones in Fig. 6).

At this point, (8)-(12) can be solved for any given i_{ph}^* and the value of $B_{st}(i_{ph}^*)$ is then easily obtained. By assuming that all coils of the same phase are series-connected, $\Psi_{ph}(i_{ph}^*, \theta_a)$ may be obtained via (13):

$$\Psi_{ph}\left({i_{ph}}^*, \theta_a\right) = \frac{2\,P\,N\,B_{st}\,L_{stk}D_s\,\beta_{st}}{2} \tag{13}$$

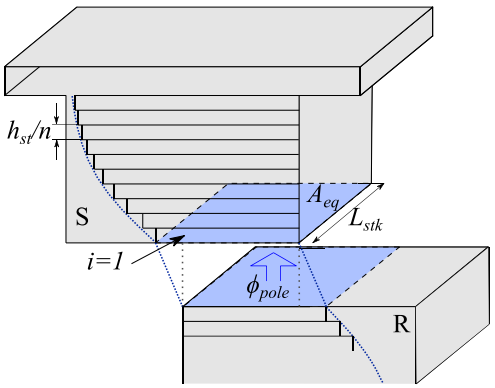

Fig. 8. Example of stator tooth flux tube discretisation at mid-way position.

Airgap Factor

The concept of airgap factor K_g, also known as Carter's factor, is well known in literature and is used for taking into account the magnetic voltage drop caused by the fringing flux in the airgaps.

At the aligned position, Ψ_{ph} can be evaluated through (7)-(13). On the other hand, at a low i_{ph}^* and hence no saturation, Ψ_{ph} may be also obtained from L_a^u (previously evaluated in the "Unsaturated Inductances" block of Fig. 3). Therefore, $K_g(\theta_a)$ may be found by equalling Ψ_{ph} obtained via (7)-(13) to the product $L_a^u\ i_{ph}^*$. In absence of saturation, iron paths' magnetic voltage drops are negligible, so that (7)-(12) simplify into (14):

$$2N i_{ph}^* = 2\frac{B_g}{\mu_0} l_g = 2\frac{B_{st}\ K_g(\theta_a)}{\mu_0} l_g \tag{14}$$

At this point, the value of B_{st} can be extracted from (14) and plugged into (13) to find Ψ_{ph}. As already mentioned, this last can be also written as $L_a^u\ i_{ph}^*$, resulting in:

$$K_g(\theta_a) = \frac{\dfrac{P\ N^2\ \mu_0\ L_{stk} D_s\ \beta_{st}}{l_g}}{L_a^{\ u}} \tag{15}$$

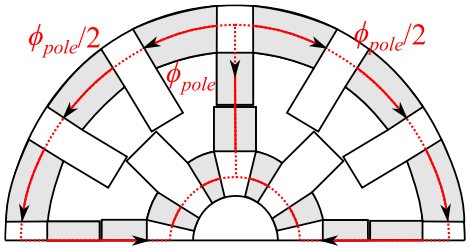

Fig. 6. Representative flux tube at the aligned, saturated conditions.

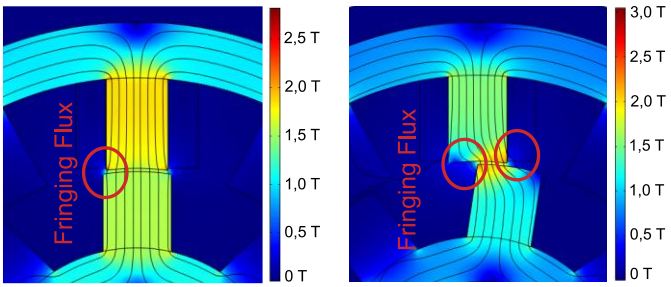

(a) (b)

Fig. 7. Magnetic Flux Density and Flux Lines distribution at the aligned position (a) and mid-way position (b).

Another interpretation of $K_g(\theta_a)$ can be given in relation to (12). Based on the Gauss' law, ϕ_{pole} is a constant, so that for stator tooth and airgap, one finds:

$$\phi_{pole} = B_{st}\ A_{st} = B_g\ A_{eq}(\theta_a) \tag{16}$$

where $A_{eq}(\theta_a)$ denotes an equivalent airgap cross section that takes the fringing flux into account. Therefore, by observing (12), it is found that $K_g(\theta_a)$ also represents the ratio between A_{st} and $A_{eq}(\theta_a)$.

$$K_g(\theta_a) = \frac{A_{st}}{A_{eq}(\theta_a)} \tag{17}$$

At this point, it is noticed that (17) is slightly different from the traditional definition of Carter's factor, as the numerator should be an average airgap cross section, taken in between stator and rotor, rather than A_{st}. This alternative formulation is used in this work only at maximum alignment, as it simplifies the mathematical formulation. For the mid-way position, the conventional definition will be used.

B. Mid-Way Position

An example of flux density and flux lines at mid-way position is shown in Fig. 7(b). As it can be noted, the main challenge in modelling this magnetic behaviour stems from the uneven flux density distribution within stator and rotor teeth, with flux lines that can no longer be approximated as straight lines. To provide a relatively simple approximation to this behaviour, this work proposes a discretisation of stator and rotor teeth in a suitably large number n of planar active slices conveying all the magnetic flux, as shown in Fig. 8. Further into detail, this simplification assumes all magnetic flux passing through the flux tube enclosed by the profile defined in (*19*), with a constant magnetic flux density inside each slice, whereas in real cases the magnetic flux crosses the entire cross section – including the teeth corner – and the magnetically equipotential surfaces are not planar.

In the case of the stator teeth, as one moves from the airgap towards the yoke, the ith slice possesses the following thickness l_i and cross section A_i:

$$l_i = \frac{h_{st}}{n} \tag{18}$$

$$A_i = A_{eq} + \left(A_{st} - A_{eq}\right) tanh\left(\frac{2(i-1)}{n}\right) \tag{19}$$

As it may be noted, the cross section is modelled via a hyperbolic tangent shape. This choice has been made due to the similarity with flux lines observed in FEA results. Moreover, the 1st segment of stator and rotor, along with the airgap, possess an equivalent cross section $A_{eq}(\theta_m)$ that takes fringing flux effects into account. Its value is obtained through the airgap factor at the mid-way position $K_g(\theta_m)$, based on the definition given in (17):

$$A_{eq}(\theta_m) = \frac{\dfrac{D_s}{4}\ \beta_{st}\ L_{stk}}{K_g(\theta_m)} \tag{20}$$

Hence, $K_g(\theta_m)$ can be obtained in the same manner as in the aligned position in (15):

$$K_g(\theta_m) = \frac{\frac{PN^2\mu_0 L_{stk} D_s \beta_{st}}{2\, l_g}}{L_m{}^u} \tag{21}$$

Regarding (20), it should be noted that the numerator is equal to half the stator tooth cross section, as it would correspond to the actual overlapping surface at θ_m. In other terms, this time the Carter's factor follows the traditional definition.

For the rotor teeth, a similar discretisation is adopted by using expressions analogous to (18) and (19).

Another point to note is related to the final segments corresponding to i=n in (19). Here, given that n is sufficiently large, the cross section is almost equal to A_{st}. Besides, it is worth noting that the factor 2 in the hyperbolic tangent argument in (19) has been selected to optimise the accuracy of the proposed method, whilst minimising the computation time.

At this point, Ampere's and Gauss' equations can be written as in (22)-(27), where $A_{eq}(\theta_m)$ is taken as a reference for ϕ_{pole}:

$$\begin{aligned} 2N i_{ph}{}^* = {} & 2\left(\sum_{i=1}^{n}\left(\frac{(B_{st})_i}{(\mu_{st})_i}\right)\right) h_{st} + 2\frac{B_g}{\mu_0} l_g \\ & + 2\left(\sum_{i=1}^{n}\left(\frac{(B_{rt})_i}{(\mu_{rt})_i}\right)\right) h_{rt} + \frac{B_{sy}}{\mu_{sy}} l_{sy} \\ & + \frac{B_{ry}}{\mu_{ry}} l_{ry} \end{aligned} \tag{22}$$

$$(B_{st})_i = \frac{(B_{st})_1}{1 + \left(\frac{A_{st}}{A_{eq}(\theta_m)} - 1\right) tanh\left(\frac{2(i-1)}{n}\right)} \tag{23}$$

$$(B_{rt})_i = \frac{(B_{st})_1}{1 + \left(\frac{\frac{D_r}{2}\,\beta_{rt}\, L_{stk}}{A_{eq}(\theta_m)} - 1\right) tanh\left(\frac{2(i-1)}{n}\right)} \tag{24}$$

$$B_{sy} = \frac{D_s\, \beta_{st}}{8\, b_{sy}} \frac{(B_{st})_1}{K_g(\theta_m)} \tag{25}$$

$$B_{ry} = \frac{D_s\, \beta_{st}}{8\, b_{ry}} \frac{(B_{st})_1}{K_g(\theta_m)} \tag{26}$$

$$B_g = (B_{st})_1 \tag{27}$$

Then, (22)-(27) can be solved numerically for any given $i_{ph}{}^*$. In particular, $(B_{st})_1$ in (27) denotes the magnetic flux density at the lowest stator tooth segment. From its value, $\Psi_{ph}(i_{ph}{}^*, \theta_m)$ may be obtained via (28):

$$\Psi_{ph}\left(i_{ph}{}^*, \theta_m\right) = \frac{2\, P\, N\, i_{ph}{}^*\, (B_{st})_1\, L_{stk} D_s\, \beta_{st}}{4\, K_g(\theta_m)} \tag{28}$$

V. Non-Linear Flux Linkage Loci Model

This section describes the idea proposed for the interpolation technique of the $\Psi_{ph}([i_{ph}], \theta)$ curves.

Before starting with the model description, it shall be noticed that for the proposed interpolation process, rather than using directly the flux linkage values, it is preferred to pass through the incremental inductance values, as it simplifies the formulation. In particular, the idea is to define a set of

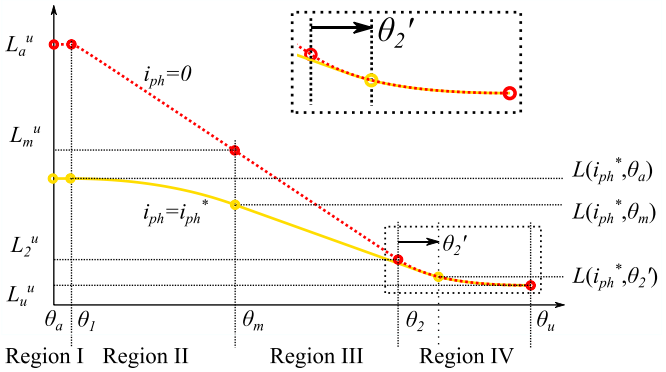

Fig. 9. Example of inductance vs rotor position curve in unsaturated and saturated conditions.

inductance vs. θ curves for discrete phase currents $L_{ph}([i_{ph}], \theta)$, from which the evaluation of the set of $\Psi_{ph}([i_{ph}], \theta)$ curves is straightforward. An example of saturated inductance curve is shown in Fig. 9 (yellow curve).

A. Saturated Inductance Profile: Region I

Even in saturated conditions, aiming to minimize the model complexity, it is commonly accepted to neglect the effects of fringing flux and rounding phenomena in this area. Hence, the inductance in this region is constant and equal to the value at maximum alignment:

$$L_{ph}\left(i_{ph}{}^*, \theta\right) = \frac{\Psi_{ph}\left(i_{ph}{}^*, \theta_a\right)}{i_{ph}{}^*} \qquad \theta_a \le \theta < \theta_1 \tag{29}$$

It is observed that in (29), $\Psi_{ph}(i_{ph}{}^*, \theta_a)$ represents the flux linkage at a given $i_{ph}{}^*$ and θ_a, evaluated in subsection IV-A.

B. Saturated Inductance Profile: Region II

Region II represents the first half of the partial overlap region, i.e., between θ_1 and θ_m. In this region, the magnetic behaviour is dominated by bulk saturation effects, producing relatively uniform saturation levels within teeth and yokes. This results in a nonlinear trend of the inductance curve at relatively high current levels, as represented in Fig. 9. In order to model this nonlinearity, the aforesaid second-order FK equation (3) is set by imposing the boundary conditions in (30).

$$\begin{cases} L_{ph}\left(i_{ph}{}^*, \theta_1\right) = \dfrac{\Psi_{ph}\left(i_{ph}{}^*, \theta_a\right)}{i_{ph}{}^*} \\ L_{ph}\left(i_{ph}{}^*, \theta_m\right) = \dfrac{\Psi_{ph}\left(i_{ph}{}^*, \theta_m\right)}{i_{ph}{}^*} \\ \dfrac{d}{d\theta}\left(L_{ph}\left(i_{ph}{}^*, \theta\right)\right)\Big|_{\theta_1} = 0 \\ \dfrac{d}{d\theta}\left(L_{ph}\left(i_{ph}{}^*, \theta\right)\right)\Big|_{\theta_m} = \\ = \dfrac{L_{ph}\left(i_{ph}{}^*, \theta_m\right) - L_{ph}\left(i_{ph}{}^*, \theta_2{}'\left(i_{ph}{}^*\right)\right)}{\theta_m - \theta_2{}'\left(i_{ph}{}^*\right)} \end{cases} \tag{30}$$

In particular, the fourth boundary condition sets the derivative equal to the slope of the profile in Region III. Here, two observations are needed: 1) Rotor position $\theta_2'(i_{ph}^*)$ is different from θ_2 and is a function of i_{ph}^*, as discussed in the next subsection, and 2) $\Psi_{ph}(i_{ph}^*, \theta_m)$ appearing in the second equation of (30) represents the flux linkage at a given i_{ph}^* and θ_m, evaluated in subsection IV-B.

C. Saturated Inductance Profile: Region III

Region III represents the second half of the partial overlap region, spanning from θ_m to θ_2'. In this region, the magnetic behaviour is dominated by local saturation effects, which arise mostly in the vicinity of the teeth corners. In real conditions, the passage from the bulk saturation typical of Region II to this new condition is progressive. However, in a bid to reflect this behaviour in a simplified mathematical way, the mid-way position θ_m has been chosen to mark the passage from one behaviour to another. Then, the smoothness of the transition is ensured by imposing the continuity of the profile's derivative at either side of θ_m, as it can be seen in the following.

The reason why θ_2' is used in-lieu of θ_2 is now explained. The absence of bulk saturation in Region III permits to approximate it through a linear trend (see Fig. 9). On the other hand, with relatively high currents, corner saturation effects are observable even at position θ_2, as it can be seen in Fig. 9, where the saturated profile at position θ_2 stands below the unsaturated one (red dotted curve). To take this effect into account, Region III is prolonged up to a new rotor position, i.e., $\theta_2'(i_{ph}^*)$. This last is found by imposing the following geometrical constraints (see Fig. 9): 1) The inductance profile of Region III must pass through the mid-way inductance point $L(i_{ph}^*, \theta_m)$, and 2) Inductance profile is tangent to the unsaturated profile of Region IV (red dotted line), previously introduced in subsection III-C.

D. Saturated Inductance Profile: Region IV

Once the position $\theta_2'(i_{ph}^*)$ has been identified, the hypothesis of negligible saturation effects in the non-overlapping zone may be made. Hence, Region IV spans between $\theta_2'(i_{ph}^*)$ and θ_u following the unsaturated profile of subsection III-C.

E. Discussion About the Proposed Profile Formulation

This subsection is devoted to a brief comparison of the interpolation technique proposed in this work against that developed in [9], whose key points are as follows: 1) Only three regions are defined, as position θ_1 is ignored. In other words, Region I proposed in this work does not exist, whereas only Region II is considered between θ_a and θ_m; 2) Both nonlinear regions (Region II and Region IV) are modelled by 1st-order FK equations.

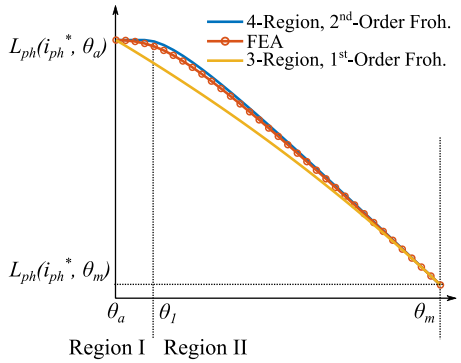

Fig. 10. Comparison between the proposed loci and the one reported in [12] in the region between θ_a and θ_m.

An example of profile proposed in this work is compared against that proposed in [9] in Fig. 10, together with FEA values. The example is taken from the SRM_A analysed in the next section at maximum rated current. Here, the first point to note is that a second-order equation allows setting a zero derivative at the fully aligned position, as opposed to the first-order counterpart, which, in turn, caters for a shape that is smoother yet closer to reality. The second point to note is concerned with the use of four regions rather than three, as keeping Region I and Region II separated sensibly increases the accuracy nearby θ_1.

VI. Model Validation And Discussion

This section is devoted to the validation and discussion of the analytical model proposed in the previous sections.

A. SRM Designs Description

As already mentioned in the introduction, the proposed model has been developed with the objective of maintaining high accuracy for SRMs featuring different geometries and conceived for different rated operating conditions. To this end, four SRM designs have been considered with very different geometric features and power ratings. From now on, designs will be referred to as SRM_A to SRM_D. Their main geometric and control parameters are listed in TABLE II, whereas Fig. 11 provides an outlook of their cross sections.

TABLE II
Geometric Parameters of the SRM Designs

	SRM_A	SRM_B	SRM_C	SRM_D
Bore Diameter [mm]	82.5	120	200	219
Outer Diameter [mm]	138	192	284	307
Stack Length [mm]	80	158	250	121
Number of Turns	4x13	2x4	2x22	4x6
Stator/Rotor Teeth	12/8	6/4	16/14	12/8
Base Speed [rpm]	1500	8000	2400	2000
DC-Link Voltage [V]	36	270	750	120
Peak Current [A]	75	600	90	350
Rated Power [kW]	1.12	40	50	20
Magnetic Material	M270	M270	M270	M270

Validation Process Description

Reminding that the analytical model has been conceived for early design stages, most of the comparisons and validation are conducted against FEA. Nonetheless, experimental results obtained from SRM_A have been also included, with the purpose of validating the FEA results, as well as assessing the discrepancy between analytical and experimental results. The SRM_A physical prototype is shown in Fig. 12.

With regards of the experimental tests, SRM_A has been run at a fixed speed measuring the instantaneous phase current and phase voltage, along with the average torque through a transducer. Eventually, instantaneous phase flux linkage and

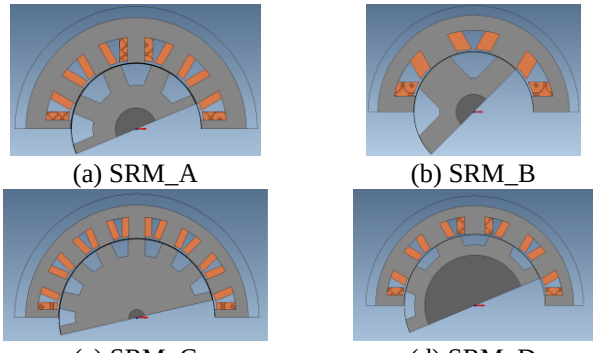

(a) SRM_A (b) SRM_B

(c) SRM_C (d) SRM_D

Fig. 11. Geometry outlook of the SRM designs used for model validation.

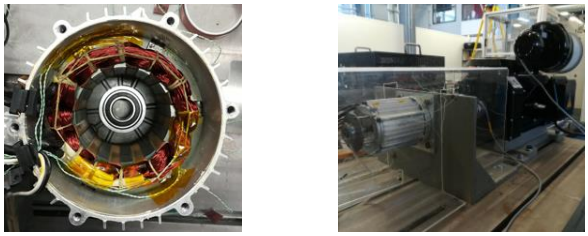

(a) (b)

Fig. 12. SRM_A Physical Prototype Outlook: (a) front view; (b) test bench.

torque have been obtained by post processing the experimental voltages and currents. More details about the FEM models, such as airgap mesh or number of nodes, as well as about the testing bench, can be found in [24].

C. Aligned and Mid-Way Flux Linkage Curves Validation

The flux linkage vs. current loci of the four designs at both aligned and mid-way rotor positions are shown in Fig. 13(a)-(d), where a very close similarity between analytical (solid lines) and FEA (dashed lines) results can be observed. Errors incurred at mid-way position are represented in Fig. 13(e) and are reported in TABLE III, where maximum, minimum and mean absolute error (||Error||) from amongst all loci points considered are shown. As it can be seen, maximum and minimum errors are well below 10%, with mean absolute errors remaining well below 5% for all designs.

In addition, by observing Fig. 13(e), for all the examined designs, the maximum positive error at θ_m is incurred in correspondence of the knee-point of the saturation curve. This discrepancy stems from the hypothesis that all magnetic flux flows in a single tube, whereas in the real case this transition is smoothed by fringing and leakage phenomena.

D. Complete Flux Linkage Loci Validation

Flux linkage loci of the four designs are shown in Fig. 14(a), (c), (e) and (g), whilst their corresponding local errors are plotted in the rotor position vs. current planes in Fig. 14 (b), (d), (f) and (h). In terms of error, TABLE IV reports the mean absolute errors from amongst all loci points considered. As it can be noted, all values are lower than 4%. Overall, bearing in mind that the process is fully analytical, the extremely good similarity with FEA proves the capability of the proposed model to suite SRM designs featuring different geometries.

TABLE III

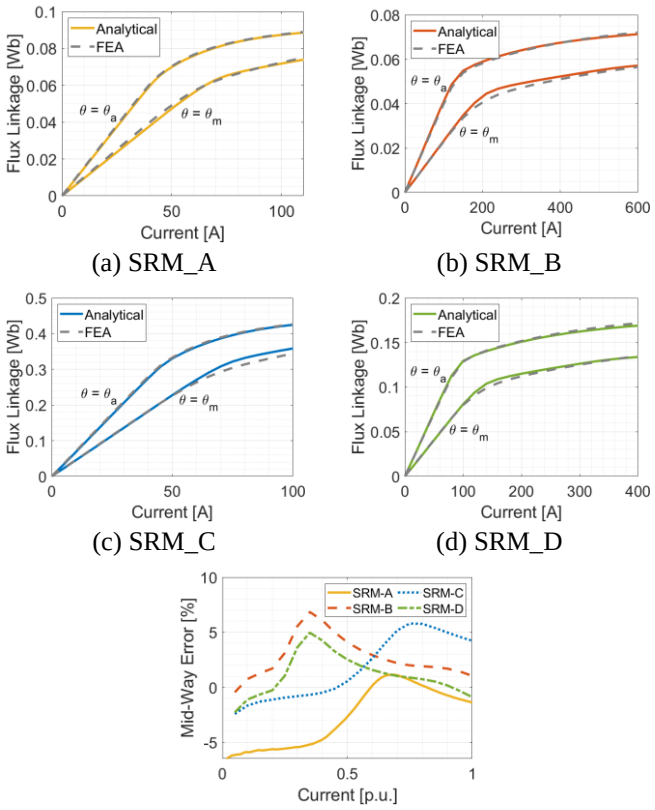

Fig. 13. Aligned and mid-way flux linkage vs. current loci, (a)-(d), and mid-way local errors (e).

MID-WAY POSITION ERRORS

	SRM_A	SRM_B	SRM_C	SRM_D
Max Error [%]	1.141	6.840	5.794	4.962
Min Error [%]	-6.486	-0.457	-2.427	-2.285
Mean ||Error|| [%]	3.090	2.679	2.693	1.698

TABLE IV
FLUX LINKAGE LOCI, MEAN ABSOLUTE ERRORS

	SRM_A	SRM_B	SRM_C	SRM_D
Mean ||Error|| [%]	3.368	3.162	2.638	3.153

E. SRM Performance Prediction Validation

In TABLE V, average torque, torque ripple and RMS currents obtained analytically, via FEA and experimentally for SRM_A are compared. As it is common practice for design processes, analytical and FEA performance have been obtained by considering a constant converter's DC-bus voltage and a hysteresis current control set to provide the desired torque. For the SRM_A, the same control parameters as in the physical prototype have been used.

In terms of average torque, errors incurred are well below 10% for all designs, even when analytical results are compared against experimental values. The flux linkage vs. current loops of the four designs are illustrated in Fig. 15(a), (c), (e) and (g). These last are reported as from their subtended

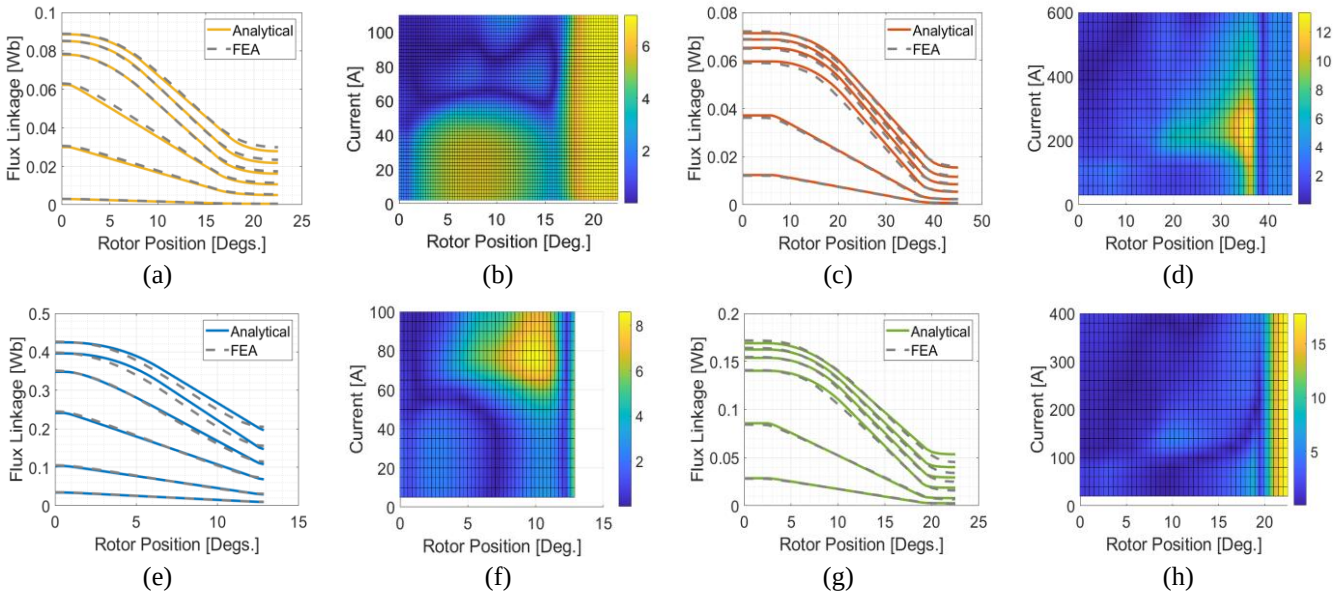

Fig. 14. Entire flux linkage loci and corresponding local errors: SRM_A (a)-(b) to SRM_D (g)-(h).

area the average torque per phase may be obtained, in accordance with the energy/coenergy theory (see (1)).

In terms of torque ripple, very good accuracy is obtained for SRM_A, SRM_B and SRM_C. For SRM_D, a 17,44% error is incurred. On the other hand, this error might still be tolerable in early design stages, as it is usually tackled at more advanced stages. Instantaneous torque waveforms are shown in Fig. 15(b), (d), (f) and (h). Finally, regarding the RMS currents, errors incurred against FEA are below 4%. With respect to the experimental value, discrepancies around 10% are obtained for both analytic and FEA results. These are mostly caused by a constant voltage drop in the physical converter prototype not considered in analytic and FEA models, as it is demonstrated in [24].

TABLE V
PERFORMANCE VALIDATION RESULTS

		Torque [Nm]	Torque Ripple [%]	Current [Arms]
SRM_A	Ana	6.430	127.61	42.006
	FEA	6.154	120.94	40.75
	Err [%]	4.485	6.670	3.082
	Exper.	6.092	132.76	37.13
	Err_{ANA} [%]	5.548	-5.150	13.132
	Err_{FEA} [%]	1.018	-11.820	9.750
SRM_B	Ana	45.059	84.91	350.884
	FEA	44.472	82.76	351.760
	Err [%]	1.320	2.15	-0.249
SRM_C	Ana	209.249	24.36	55.102
	FEA	215.294	24.80	55.234
	Err [%]	-2,808	-0,44	-0,239
SRM_D	Ana	88.628	96.50	184.997
	FEA	95.619	79.06	191.490
	Err [%]	-7.311	17,44	-3.391

F. Discussion upon Model Implementation in a Design Routine

This subsection provides a brief benchmark design exercise for SRM_A, [7], with the objective of showing the reduction in computational time obtained by using the proposed model. To this end, a Genetic Algorithm is run, set on 50 generations with 15 design candidates each. The routine is implemented in MATLAB and runs on a workstation, with an i7-3630 processor @2.40 GHz, 24 GB RAM. The computation times needed to obtain the $\Psi_{ph}([i_{ph}], \theta)$ curves of 750 candidates are compared in TABLE VI. As it can be seen, the fully analytical model allows to complete the process in less than 1 hour and is about 785 times faster than the fully FEA process.

TABLE VI
COMPUTATION TIMES COMPARISON

	Analytic	FEA
Computation time [mins]	42	37500

VII. CONCLUSION

This work proposed and developed a novel design-oriented analytical model that predicts the flux linkage loci for SRM of any geometry and rated operating conditions, from which the main SRM performance are obtained. The model capability to effectively deal with different geometries and rated operating conditions has been proven against four very different SRM designs. Moreover, when applied in a design routine, the model showed an extremely convenient trade-off between accuracy and execution time.

Based on that, the model proved to be a very interesting and useful analytical tool for SRM designers. Besides, the extremely good compromise between accuracy and execution time encourages its utilisation in automated early design stages design routines.

REFERENCES

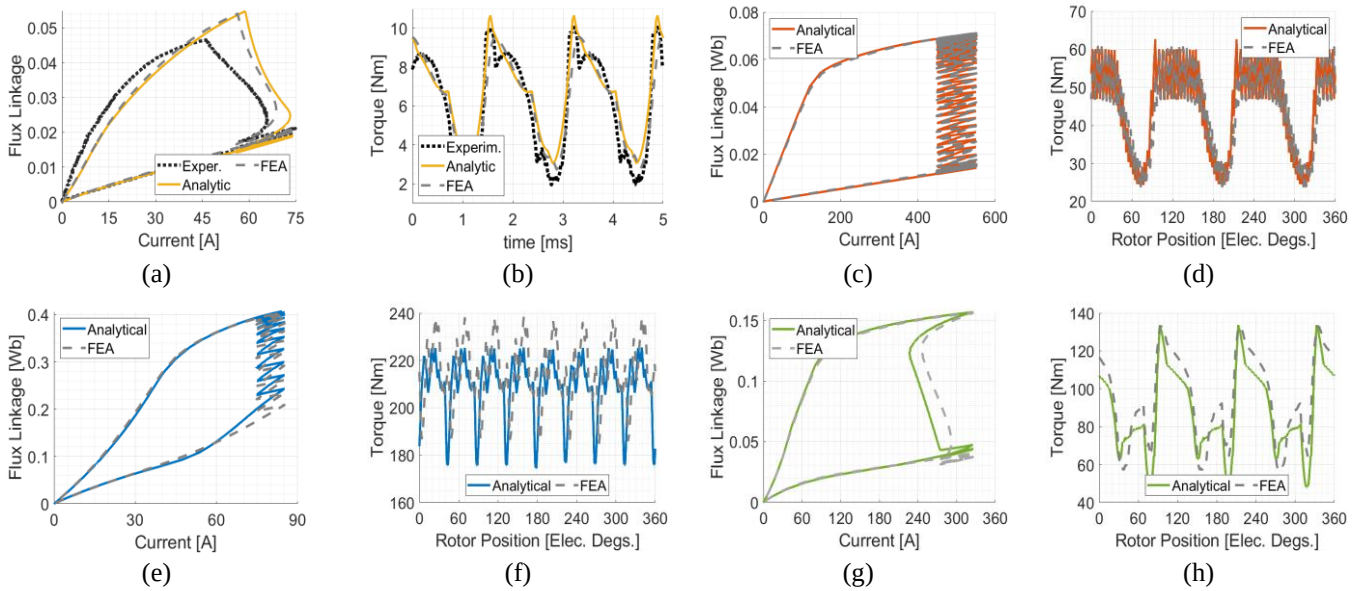

Fig. 15. Designs Performance Prediction: SRM_A (a)-(b) to SRM_D (g)-(h).

[1] S. Li, S. Zhang, T. G. Habetler, and R. G. Harley, "Modeling, Design Optimization, and Applications of Switched Reluctance Machines—A Review," *IEEE Trans Ind Appl*, vol. 55, no. 3, pp. 2660–2681, 2019, doi: 10.1109/TIA.2019.2897965.

[2] R. Rocca, S. Papadopoulos, M. Rashed, G. Prassinos, F. Giulii Capponi, and M. Galea, "Design Trade-Offs and Feasibility Assessment of a Novel One-Body, Laminated-Rotor Flywheel Switched Reluctance Machine," *Energies* , vol. 13, no. 22. 2020. doi: 10.3390/en13225857.

[3] C. Ho, J. Wang, K. Hu, and C. Liaw, "Development and Operation Control of a Switched-Reluctance Motor Driven Flywheel," *IEEE Trans Power Electron*, vol. 34, no. 1, pp. 526–537, 2019, doi: 10.1109/TPEL.2018.2814790.

[4] K. Diao, X. Sun, G. Lei, Y. Guo, and J. Zhu, "Multiobjective System Level Optimization Method for Switched Reluctance Motor Drive Systems Using Finite-Element Model," *IEEE Transactions on Industrial Electronics*, vol. 67, no. 12, pp. 10055–10064, 2020, doi: 10.1109/TIE.2019.2962483.

[5] K. Diao, X. Sun, G. Lei, Y. Guo, and J. Zhu, "Multimode Optimization of Switched Reluctance Machines in Hybrid Electric Vehicles," *IEEE Transactions on Energy Conversion*, vol. 36, no. 3, pp. 2217–2226, 2021, doi: 10.1109/TEC.2020.3046721.

[6] S. Li, S. Zhang, C. Jiang, J. Rhett Mayor, T. G. Habetler, and R. G. Harley, "A fast control-Integrated and multiphysics-Based multi-Objective design optimization of switched reluctance machines," in *2017 IEEE Energy Conversion Congress and Exposition, ECCE 2017*, 2017. doi: 10.1109/ECCE.2017.8095857.

[7] R. Rocca *et al.*, "Actual Design Space Methodology for Preliminary Design Analysis of Switched Reluctance Machines," *IEEE Trans Ind Appl*, vol. 57, no. 1, pp. 397–408, 2021, doi: 10.1109/TIA.2020.3038352.

[8] S. Zhang, S. Li, R. G. Harley, and T. G. Habetler, "An Efficient Multi-Objective Bayesian Optimization Approach for the Automated Analytical Design of Switched Reluctance Machines," in *2018 IEEE Energy Conversion Congress and Exposition, ECCE 2018*, 2018. doi: 10.1109/ECCE.2018.8557480.

[9] T. J. E. Miller and M. McGilp, "Nonlinear theory of the switched reluctance motor for rapid computer-aided design," *IEE Proceedings B Electric Power Applications*, vol. 137, no. 6, p. 337, 1990, doi: 10.1049/ip-b.1990.0042.

[10] J. M. Stephenson and J. Čorda, "Computation of torque and current in doubly salient reluctance motors from nonlinear magnetisation data," *Proceedings of the Institution of Electrical Engineers*, vol. 126, no. 5, p. 393, 1979, doi: 10.1049/piee.1979.0095.

[11] D. N. Essah and S. D. Sudhoff, "An improved analytical model for the switched reluctance motor," *IEEE Transactions on Energy Conversion*, vol. 18, no. 3, pp. 349–356, Sep. 2003, doi: 10.1109/TEC.2003.815825.

[12] A. Khalil and I. Husain, "A fourier series generalized geometry-based analytical model of switched reluctance machines," *IEEE Trans Ind Appl*, vol. 43, no. 3, pp. 673–684, May 2007, doi: 10.1109/TIA.2007.895737.

[13] S. Song, M. Zhang, and L. Ge, "A new decoupled analytical modeling method for switched reluctance machine," *IEEE Trans Magn*, vol. 51, no. 3, Mar. 2015, doi: 10.1109/TMAG.2014.2363214.

[14] F. R. Salmasi and B. Fahimi, "Modeling switched-reluctance machines by decomposition of double magnetic saliencies," *IEEE Trans Magn*, vol. 40, no. 3, pp. 1556–1561, May 2004, doi: 10.1109/TMAG.2004.826624.

[15] A. Stuikys, B. Zaghari, and J. K. Sykulski, "Instantaneous Electromagnetic Torque Waveform Calculations for Switched Reluctance Machines Exploiting Vector Analysis," *IEEE Trans Magn*, vol. 57, no. 1, Jan. 2021, doi: 10.1109/TMAG.2020.3034565.

[16] A. E. Kennelly, "Magnetic reluctance," *Transactions of the American Institute of Electrical Engineers*, vol. 8, no. 1, pp. 483–533, Jan. 1891, doi: 10.1109/T-AIEE.1891.5570158.

[17] A. Stuikys and J. K. Sykulski, "An Efficient Design Optimization Framework for Nonlinear Switched Reluctance Machines," *IEEE Trans Ind Appl*, vol. 53, no. 3, pp. 1985–1993, May 2017, doi: 10.1109/TIA.2017.2665345.

[18] R. Rocca, F. G. Capponi, S. Papadopoulos, G. De Donato, M. Rashed, and M. Galea, "Optimal Advance Angle for Aided Maximum-Speed-Node Design of Switched Reluctance Machines," *IEEE Transactions on Energy Conversion*, vol. 35, no. 2, pp. 775–785, 2020, doi: 10.1109/TEC.2019.2959823.

[19] J. M. Kokernak and D. A. Torrey, "Magnetic Circuit Model for the Mutually Coupled Switched-Reluctance Machine," 2000.

[20] W. Uddin and Y. Sozer, "Analytical Modeling of Mutually Coupled Switched Reluctance Machines under Saturation Based on Design Geometry," *IEEE Trans Ind Appl*, vol. 53, no. 5, pp. 4431–4440, Sep. 2017, doi: 10.1109/TIA.2017.2714627.

[21] A. Radun, "Analytically computing the flux linked by a switched reluctance motor phase when the stator and rotor poles overlap," *IEEE Trans Magn*, vol. 36, no. 4 PART 2, pp. 1996–2003, 2000, doi: 10.1109/20.875277.

[22] A. Stuikys and J. Sykulski, "Rapid multi-objective design optimisation of switched reluctance motors exploiting magnetic flux tubes," *IET Science, Measurement and Technology*, vol. 12, no. 2, pp. 223–229, Mar. 2018, doi: 10.1049/iet-smt.2017.0213.

[23] V. Vujičić and S. N. Vukosavić, "A simple nonlinear model of the switched reluctance motor," *IEEE Transactions on Energy Conversion*, vol. 15, no. 4, pp. 395–400, 2000, doi: 10.1109/60.900499.

[24] R. Rocca, "Actual Design Space Methodology for High-Performance Switched Reluctance Machines Design," Ph.D. dissertation, The University of Nottingham, 2019. doi: 10.13140/RG.2.2.29351.50083/1.